DSSC Anchoring Groups: A Surface Dependent Decision

Conn O'Rourke[*,†,‡,¶] and David R. Bowler[†,‡,¶]

London Centre for Nanotechnology, 17-19 Gordon St, London, WC1H 0AH, Department of Physics & Astronomy, University College London, Gower St, London, WC1E 6BT, and UCL Satellite, International Centre for Materials Nanoarchitectonics (MANA), National Institute for Materials Science (NIMS), 1-1 Namiki, Tsukuba, Ibaraki 305-0044, Japan

E-mail: ucapcor@live.ucl.ac.uk

---

[*]To whom correspondence should be addressed
[†]LCN
[‡]UCL
[¶]UCL Satellite, MANA

Abstract

Electrodes in dye sensitised solar cells (DSSCs) are typically nanocrystalline anatase TiO_2 with a majority (101) surface exposed. Generally the sensitising dye employs a carboxylic anchoring moiety through which it adheres to the TiO_2 surface. Recent interest in exploiting the properties of differing TiO_2 electrode morphologies, such as rutile nanorods exposing the (110) surface and anatase electrodes with high percentages of the (001) surface exposed, begs the question of whether this anchoring strategy is best, irrespective of the majority surface exposed. Here we address this question by presenting density functional theory calculations contrasting the binding properties of two promising anchoring groups, phosphonic acid and boronic acid, to that of carboxylic acid. Anchor-electrode interactions are studied for the prototypical anatase (101) surface, along with the anatase (001) and rutile (110) surfaces. Finally the effect of using these alternative anchoring groups to bind a typical coumarin dye (NKX-2311) to these TiO_2 substrates is examined. Significant differences in the binding properties are found depending on both the anchor and surface, illustrating that the choice of anchor is necessarily dependent upon the surface exposed in the electrode. In particular the boronic acid is found to show the potential to be an excellent anchor choice for electrodes exposing the anatase (001) surface.

Introduction

Titanium dioxide (TiO_2) has a wide range of practical applications; for example in photocatalysis[1,2], as a white pigment[3], photo-degradation of molecules at its surface make it useful as an anti-bacterial agent[4] and in waste water treatment[5], and of course it is used in dye sensitised solar cells[6]. Due to the number of technological uses, considerable effort has been expended in characterising the properties of TiO_2(for a review see[7]). TiO_2 surface structure and its interaction with molecules is of fundamental importance to many potential applications, not least DSSCs. This fact has acted as the driving force behind the characterisation of titania surfaces, and the study of how these surfaces and molecules interact. In this paper we examine how the binding properties of

molecules to TiO_2 surfaces depends on both the surface adhered to, as well as the anchoring group the molecule uses to bind to the surface.

Dye sensitised solar cells' efficiency relies heavily on the interplay between sensitising dye and the TiO_2 surface to which it binds. A strong interaction will ensure the dye remains bound to the surface, and good electronic overlap between the surface and dye is essential for efficient charge transfer[8]. This stresses the importance played by the anchoring moiety in a sensitising dye. Ruthenium based record efficiency dyes (N719, N3, black dye[9–11]) all contain one or more carboxylic acid binding groups, and the vast majority of sensitising dyes have followed this anchoring strategy.

Titanium dioxide exists in several polymorphs, two of which are used in DSSCs, anatase and rutile. TiO_2 in nanocrystalline form is most thermodynamically stable in its anatase phase[12], with the (101) face dominating more than 94% of the crystal surface[13]. Coupling this with the fact that most sensitising dyes use a carboxylic binding moiety, highlights the importance of the (101)-carboxylic acid interaction. Several experimental and theoretical studies have been devoted to examining the interaction of carboxylic anchors with the TiO_2 (101) surface[14,15].

However, carboxylic acid groups are not the only choice for anchoring dyes to TiO_2 surfaces, and bias towards them may be at the expense of other potentially useful candidates being neglected. Examples include phosphonic acid[16,17], boronic acid[18], and cyano-benzoic acid[19], all of which have been used as binding groups in DSSCs. Notably dyes utilising phosphonic acids have shown a stronger binding interaction with TiO_2 than carboxylic acids[17,20], suggesting an advantage over those utilising carboxylic acids. Increased binding strength could lead to higher dye uptake and enhanced longevity over carboxylic acid bound dyes, as these tend to slowly desorb from the TiO_2 surface.

In a similar vein, while the prevalence of the anatase (101) surface make it extremely important, the interaction of dyes with other TiO_2 surfaces and polymorphs should not be neglected. For example, the use of rutile TiO_2 nanorods exposing the (110) surface has been explored as a potential avenue for increased electron transport rates through the electrode, resulting from reduced grain

3

boundaries[21–23]. Also interest in the less stable (001) anatase surface is increasing due to recent work showing that electrodes exposing the (001) face significantly improves device performance as a result of enhanced light scattering and increased surface activity[24–26].

Interactions between any particular anchor group and TiO_2 will necessarily differ depending on the surface. The aim of this paper, therefore, is to assess the relative merits of three potential anchor groups when binding to these less utilised, but increasingly important, surfaces. Firstly we introduce the two most important polymorphs of TiO_2, with an examination of the three mentioned surfaces; anatase (101), anatase (001) and rutile (110). Taking each of these in turn we then investigate the adsorption of two potential anchoring groups, phosphonic acid and boronic acid, at these surfaces and contrast to that of carboxylic acid. Finally we examine the properties of a full dye, the NKX-2311 coumarin dye, bound to each of these surfaces through all three anchoring groups.

Computational Details

All the calculations in this paper have been performed using the plane wave DFT code VASP (version 5.3.3)[27]. Electron exchange and correlation was treated within the generalised gradient approximation of Perdew and Wang[28] and the pseudopotential method was utilised in the form of ultrasoft Vanderbilt pseudopotentials[29] to treat core electrons. For Titanium atoms the $4s^2 3d^2$ electrons are treated as valence electrons, for boron, oxygen, carbon and nitrogen the 1s electrons are treated as being in the core. Phosphorous atoms are treated with the $1s^2 2s^2 2p^6$ electrons considered to be in the core. Semi-local functionals such as the PW91 functional employed here are known to incorrectly describe defect states in TiO_2, such as oxygen vacancies. Hybrid functionals and GGA corrected for on-site Coulomb interactions (GGA+U) have been shown to improve the desciption of these defects, however as we are examining the interaction of adsorbates with clean TiO_2 surfaces we restrict our approch to that of the pure GGA functional.

Sampling of the reciprocal space is performed using a Monkhorst-Pack k-point grid. For the

bulk calculations we have employed a k-point mesh of $(6 \times 6 \times 3)$ and $(3 \times 3 \times 6)$ for anatase and rutile respectively. Total fixed-volume energies at a cut-off of 450 eV are found to be converged to within 17 meV of those obtained at a cut-off of 650 eV for both rutile and anatase. During the calculation of the lattice parameters the higher cut-off of 650 eV has been used to ensure accuracy. Structural relaxation is performed using the RMM-DIIS[30] method until the forces on free ions were less than 0.005 eV/Å for bulk calculations. Calculated bulk lattice parameters a & c show good agreement with experiment[31] and previous computational work[13], and are 3.817Å & 9.737Å for anatase and 4.602Å & 2.949Å for rutile.

For the surface and molecular adsorption calculations the lesser 450 eV cut-off has been used, along with a less stringent maximum force criterion of 0.03 eVÅ^{-1}. Similarly the k-point mesh density has been reduced to 1 perpendicular to the surface. In order to replicate the bulk, the bottom layer of the anatase slabs have been restrained to remain in the bulk position. For rutile we have also performed calculations with the bottom layer free to relax.

In all surface and adsorption calculations, in order to prevent spurious interactions between adjacent images, the cell size is such that at least 9Å of vacuum separates periodic slab images (and adjacent molecules in adsorption calculations).

TiO$_2$ Surfaces

In order to obtain an accurate picture of the molecular adsorption at TiO$_2$ surfaces, it is important to converge the surface properties with respect to the number of layers in our slab model. In this section we characterise the anatase (101), anatase (001) and rutile (110) surfaces and converge the surface properties to an acceptable level so as to accurately examine the more computationally demanding molecular adsorptions yet to be performed with minimum computational effort.

Anatase (101)

On formation of the stoichiometric (101) surface both fivefold-coordinated titanium (Ti(5)) and twofold-coordinated oxygen (O(2)) atoms become exposed. Also present in the topmost layer are O(3) and the less exposed Ti(6) atoms, figure 1.

The displacements resulting from surface relaxation in the [101] and [10$\bar{1}$] directions of the topmost atoms for three and six layer slabs can be seen in figure 1. Most notable are the large outward displacement of the O(3ii) and inward displacement of the Ti(5) atoms in the [101] direction. A more jagged surface along the [010] direction, with the O(3ii) atom protruding beyond the Ti(5) atom, results.

Important also is the reduction in length and change of direction of the O(2)-Ti(6) bond, from 1.95 (Å) to 1.87 (Å), as a result of the substantial outward [101] relaxation of the Ti(6) atom and large displacement in the [10$\bar{1}$] direction of the O(2) atom. These surface characteristics reproduce well those found in other studies using the PBE functional[13].

Surface formation energies have been calculated by the subtraction of the bulk energy per layer times the number of layers from the total energy obtained, and dividing by the total exposed area, 2A (1a). Relaxed surface energies are then computed by subtraction of the energy change on relaxation per unit area from this unrelaxed surface energy (1b). Both relaxed and unrelaxed surface energies for slabs of varying thickness are presented in table 1(i).

$$E_{unrel} = \frac{1}{2A}[E_{un}^{Tot} - nE_{bulk}] \tag{1a}$$

$$E_{rel} = [E_{unrel} - \frac{\Delta E}{A}] \tag{1b}$$

For the six layer slab good agreement is found between the calculated unrelaxed (relaxed) surface energies of 1.267 J/m^2 (0.537 J/m^2) and that of previous work for a six layer slab using the PBE functional, 1.28 J/m^2 (0.49 J/m^2)[13].

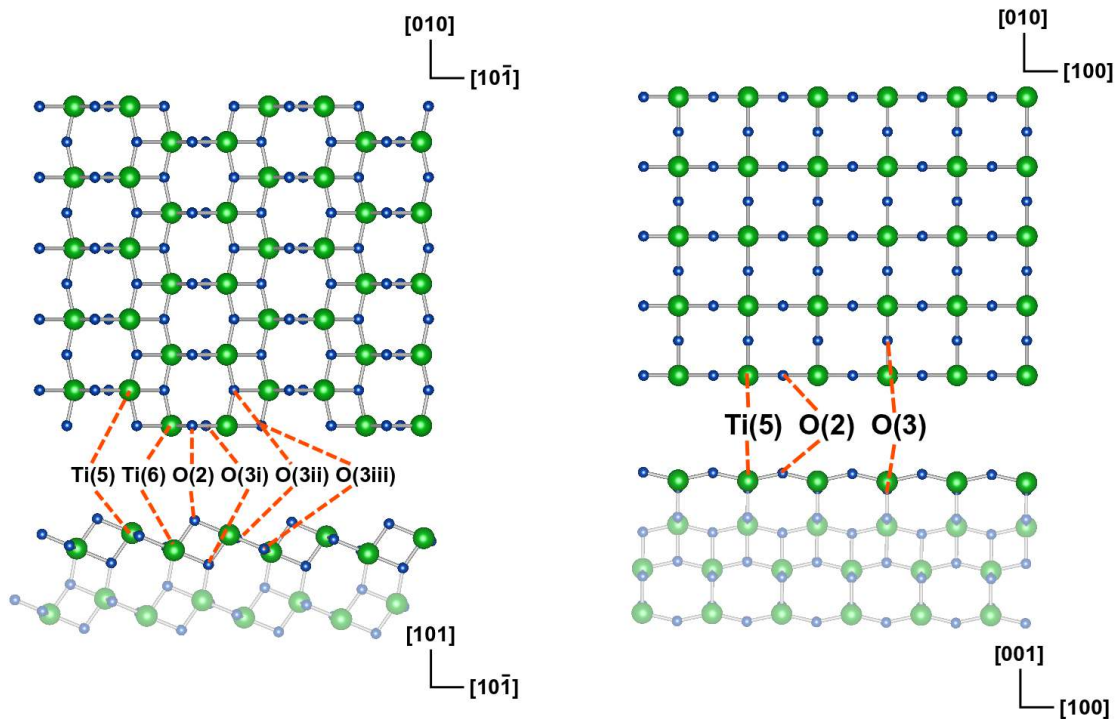Unrelaxed (relaxed) surface formation energies for the three layer slab are found to be con-

6

Figure 1: Anatase surfaces: (101) left and (001) right. Titanium atoms are green, oxygen atoms are blue. Both top views (top) and side views (bottom) are included, with coordination of surface atoms labelled.

verged to within 0.01 J/m^2 (0.015 J/m^2) with respect to that of the six layer slab. Although the convergence of relaxation displacements for the three layer representation are not as tight, it can be seen that the three layer model does qualitatively reproduce to a good degree the characteristic displacements found in the six layer slab. As a trade-off between computational ease and accuracy we have opted for the three layer TiO$_2$ (101) slab for the calculations involving adsorption of molecules.

Anatase (001)

The unreconstructed (001) surface is reported to be much less stable than the (101) surface[13,32]. However based on a Wulff construction it has been shown that for anatase nanocrystals, although comprising a much smaller area than the majority (101) surface, the (001) crystal face will still be exposed[13] in agreement with experiment.

Table 1: Anatase (101) Surface: (i) Relaxed and unrelaxed surface energies for different layer anatase slabs (ii) Displacements from bulk position on relaxation of Anatase (101) surface for 3 layer slab (values for 6 layer slab are shown in brackets)

N_{lay}	Surface Energy	
	E_{unrel} (J/m^2)	E_{rel} (J/m^2)
3	1.259	0.522
4	1.260	0.514
5	1.260	0.534
6	1.267	0.537

(i)

	Atomic Disp. (Å)	
Label	[10$\bar{1}$]	[101]
Ti(5)	-0.114 (-0.131)	-0.101 (-0.140)
Ti(6)	0.027 (0.012)	0.207 (0.154)
O(2)	0.140 (0.117)	0.017 (0.031)
O(3i)	0.031 (0.030)	-0.005 (-0.051)
O(3ii)	0.051 (0.030)	0.262 (0.219)
O(3iii)	-0.002 (-0.020)	0.081 (0.034)

(ii)

Cleaving the anatase lattice perpendicular to the (001) surface exposes both two-fold and three-fold coordinated oxygen atoms, as seen in figure 1. In contrast to the (101) surface however, the O(2) atoms number ½ of those oxygen atoms exposed in the surface (for the (101) surface O(2) atoms make up ⅓). Similarly the (001) surface exposes only Ti(5) atoms, as opposed to the (101) surface which expose equal numbers of Ti(5) and Ti(6), as seen in 1. The high proportion of under-coordinated atoms in the (001) surface goes some way to explain its reported high reactivity[33,34].

It is this high reactivity that makes the (001) surface of interest for many applications such as photocatalysis and photo-degradation of organic molecules[34–36]. Recent work has shown that it is possible to increase the exposed percentage of the (001) surface by, for example, using hydrofluoric acid as a capping agent, thus improving its photocatalytic properties[35]. Similarly increasing the percentage of the exposed (001) face has been shown to improve DSSC performance[37]. Several reasons for this improvement have been suggested, such as the increased reactivity leading to higher dye adsorption, improved light scattering properties, and improved crystallinity leading to lower recombination rates[37–39].

Calculated surface energies for the (001) surface are presented in table 2, and can be seen to be significantly higher than those of the (101) surface, as expected. Our calculated value of 1.145 J/m^2 (1.06 J/m^2) for the unrelaxed (relaxed) surface energy of the 4 layer slab is in good agreement with the result of 1.12 J/m^2 (0.98 J/m^2) reported elsewhere[13]. It can be seen that the relaxed surface

energies are converged to within 0.004 J/m^2 for a four layer slab compared to those calculated for a seven layer slab, and we employ the four layer slab for the calculations involving molecular adsorption.

Table 2: Anatase (001) Surface: (i) Relaxed and unrelaxed surface energies for different layer anatase slabs (ii) Displacements from bulk position on relaxation of Anatase (001) surface for 3 layer slab (values for 7 layer slab are shown in brackets)

N_{lay}	Surface Energy	
	E_{unrel} (J/m^2)	E_{rel} (J/m^2)
2	1.172	1.053
3	1.220	1.054
4	1.145	1.060
5	1.146	1.060
6	1.144	1.055
7	1.144	1.056

(i)

Label	Atomic Disp. (Å)
	[001]
Ti(5)	-0.047 (+0.048)
O(2)	+0.046 (+0.034)
O(3)	+0.020 (-0.010)

(ii)

Atomic displacements for the surface atoms in the [001] direction are also given in table 2, and agree well with previous work[13]. Along the [100] direction we find that in order to obtain the broken symmetry surface solution reported elsewhere[13], with the Ti(5)-O(2)-Ti(5) bonds extending and shortening respectively to 2.20Å and 1.76Å, we require a larger simulation cell than the (1 × 1×1) here. Indeed this symetry breaking was also found in larger supercells used for the adsorption of acidic binding groups, with the Ti(5)-O(2) bond lengths changing to 2.20 and 1.78Å.

Rutile (110)

Typical DSSC electrodes are composed of nanocrystalline TiO$_2$ particles, in anatase form. Grain boundaries between the crystals can lead to high rates of recombination and low electron diffusion coefficients. One potential approach to minimise this effect has been to construct single crystalline rutile nanorods, reducing the grain boundaries and improving electron transport[40] and also leading to increased surface areas, thereby improving dye take-up[41]. Grown along the [001] direction these nanorods expose a majority (110) surface for dye adsorption[22,42], highlighting the importance of the interaction between the (110) surface and potential dye anchors.
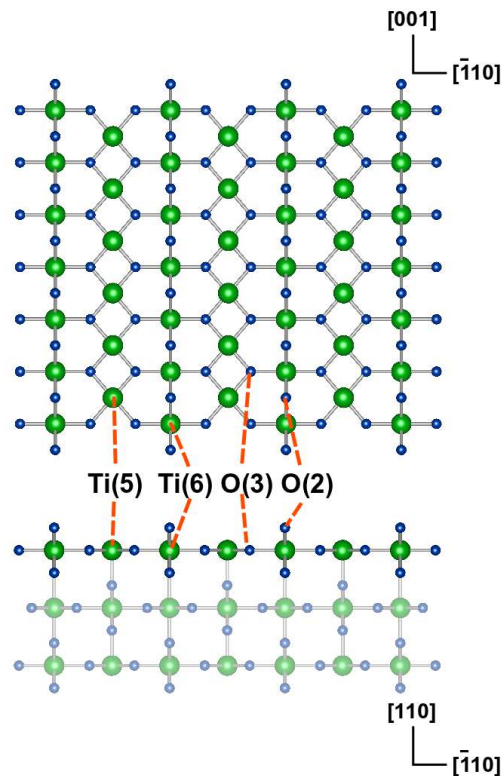
Figure 2: Rutile (110) surfaces: Titanium atoms are green, oxygen atoms are blue. Both top view (top) and side view (bottom) are included, with coordination of surface atoms labelled.

Forming a stoichiometric surface by truncating the bulk rutile structure along the [110] direction exposes both fully coordinated O(3) and undercoordinated O(2) atoms, as can be seen in figure 2. Similarly both fully coordinated and under-coordinated Ti(5) and Ti(6) atoms are exposed.

Examining the rutile slab we can see that it has an alternating bi-periodic layer structure; in the bottom of figure 2 it can be seen that the inclusion of each additional layer causes the position of the exposed O(2) along the $[1\bar{1}0]$ direction to alternate, such that they coincide by layer with period two. This alternating structure leads to the surface properties of rutile (110) being slower to converge with respect to slab thickness when compared to other TiO_2 surfaces. As such we have examined the effects of two methods; full relaxation of the entire slab (FR) and fixing the bottom surface to the bulk positions (BF).

Calculated surface energies for both systems can be seen in table 3. As discussed elsewhere there are a wide range of theoretical values reported for rutile (110) surface energies[43], hinting at

the difficulty in converging the properties of this surface. We see that the surface energies for slabs with the bottom layer fixed converge to a value in the region of $\sim$ 0.36-0.39 eV, with a significant number of layers required in order to reach this convergence. The fully relaxed slab converges more slowly, seemingly reaching a much higher converged energy of $\sim$ 0.49-0.50 eV after 12 layers. We would suggest that increasing the number of layers further should cause the surface energy to approach that of the fully relaxed slab, but comes with significant computational expense. Another point to note is that both relaxed surface energies for the FR and BF slabs converge bi-periodically, following the same pattern as the surface structure. Examining the atomic displacements for the BF and FR slabs in table 3(ii), we see that both methods show the same displacement trends in the [110] direction as experiment, and the 4 layer slab in both cases is well converged with respect to the 11 layer slab, illustrating that the effect of the bi-periodic structure is minimised as the thickness increases.

Table 3: Rutile (110) Surface: (i) Relaxed and unrelaxed surface energies for different layer rutile slabs (BF is with the bottom fo the slab fixed, FR is total relaxation). (ii) Displacements from bulk position on relaxation of Rutile (110) surface for 4 layer slab (values for 11 layer slab are shown in brackets)In both (i) & (ii) BF stands for the bottom of the slab fixed, while FR is total relaxation.

N_{lay}	Surface Energy		
	E_{unrel} (J/m^2)	$E_{rel}(BF)$ (J/m^2)	$E_{rel}(FR)$ (J/m^2)
3	1.448	0.681	0.771
4	1.421	0.333	0.444
5	1.429	0.495	0.603
6	1.427	0.345	0.473
7	1.429	0.426	0.560
8	1.427	0.360	0.492
9	1.427	0.402	0.532
10	1.424	0.363	0.499
11	1.423	0.392	0.525
12	1.423	0.373	0.503

(i)

Label	Atomic Disp. (Å)		
	[110](BF)	[110] FR	Expt[44]
Ti(6)	+0.265(+0.247)	+0.292(+0.216)	+0.25 ±0.03
Ti(5)	-0.154(-0.186)	-0.186(-0.193)	-0.19 ±0.03
O(2)	+0.053(+0.037)	+0.079(+0.005)	+0.10 ±0.05
O(3)	+0.188(+0.149)	+0.160(+0.142)	+0.17 ±0.08

(ii)

As mentioned, reported values for the relaxed and unrelaxed surface energies show a wide variation depending on the approach and number of layers used[43]. Previous work with the LDA

functional for a fully relaxed slab of 6 layer thickness reports a values of 1.78 J/m^2 and 0.84 J/m^2 for the relaxed and unrelaxed surface energies, while using GGA-PBE the values reported are 1.38 and 0.35 J/m^2 respectively[13]. These values are in reasonable agreement with those for our fully relaxed 6 layer slab of 1.427 J/m^2 and 0.473 J/m^2. Again highlighting the dependence of the (110) surface energies on the approach used, in reference[43] the reported values differ by around 0.1eV between the GGA-PW91 functional result and that using the GGA-PBE functional, with the PW91 surface energies converging to $\sim$ 1.48 and $\sim$ 0.57 J/m^2 respectively.

Given the apparent discrepancies between much of the reported results for surface energies of the (110) surface, and focusing on the objective behind this paper, to examine the interaction of anchoring groups with the surface, we also study the convergence of two further properties. Firstly we have also looked at the convergence with slab thickness of calculated adsorption energies for two anchoring groups on the (110) surface. The two anchoring groups chosen are the boronic and formic acids groups, which can be seen in figure 4, and will be discussed further in later sections. Calculated adsorption energies for both (in a bidentate binding configuration) can be seen in table 4.

Table 4: Calculated adsorption energies for the boronic and formic acid anchoring moieties on rutile (110) surfaces of differing thickness. FR again stands for fully relaxed slabs, while BF stands for slabs with the bottom layer fixed.

| | Adsorption Energy | | | |
| | FR | | BF | |
N_{lay}	Boronic (eV)	Formic (eV)	Boronic (eV)	Formic (eV)
2	-0.104	-0.725	-0.752	-1.297
3	-3.193	-2.668	-2.523	-2.144
4	-1.018	-1.326	-1.129	-1.363
5	-2.075	-1.934	-1.707	-1.673
6	-1.344	-1.567	-1.276	-1.432
7	-2.117	-2.044	-1.469	-1.528

We can see that the convergence of the adsorption energies is also slow with respect to slab thickness, with the calculated values exhibiting large variations as the number of layers increases and also converging bi-periodically. It can be seen that the relative absorption energies for the

anchors on the fully relaxed slab vary with the slab thickness, with the boronic acid being most stable on slabs with odd layers while the formic acid is most stable on even. This is also the case for the BF slab up until around 5 layers, where there the adsorption energies are very similar. For six and seven layer slabs the general relative binding strength is consistent, with the formic acid binding more strongly. Clearly converging the properties of the rutile (110) surface has its difficulties, although from this result we can say that fixing the bottom layer aids convergence of the adsorption energies. The computational demand of simulating a slab of seven or more layers is less than ideal, and it is worth noting that a four layer slab, although not as well converged, does get the relative ordering of the anchor binding strengths correct.

Convergence of the density of states for the rutile (110) TiO_2 slabs has also been examined, in both the FR and BF variants, shown in figure 3. Wide variation in the size of the band-gap was found with the differing number of layers present, with reduced band-gaps for thin slabs.

In the case of the BF slab this reduced band gap is maintained up to 12 layers, with a band gap width of around 1.5 eV, while for a 12 layer FR slab it is around 2 eV, close to the reported GGA band gap for bulk rutile. The band gap reduction is particularly pronounced for thin slabs containing odd numbers of layers. Examining the frontier orbitals for the 3 and 5 layer slabs we found that the lowest unoccupied molecular orbital is in Ti 3d orbitals spread throughout the lattice, but with the majority localised on non-surface atoms. The highest occupied molecular orbital (HOMO) is similarly spread throughout the lattice, in oxygen 2p orbitals for the FR slab. The BF slab differs, with the HOMO localised almost exclusively on fixed oxygens in the bottom layer. This illustrates that the computational approach of fixing of the bottom layer is responsible for the artificial shortening of the band gap.

It is interesting that for the density of states the fully relaxed slab exhibited much better convergence (towards the correct bulk GGA result) than that with the bottom layer fixed, at variance with the convergence of the adsorption energies. Indeed the density of states for a 4 layer FR slab shows good agreement with that of the 12 layer slab, and has no states in the gap.

Taking into account the difficulty of converging the properties of the rutile (110) surface, we
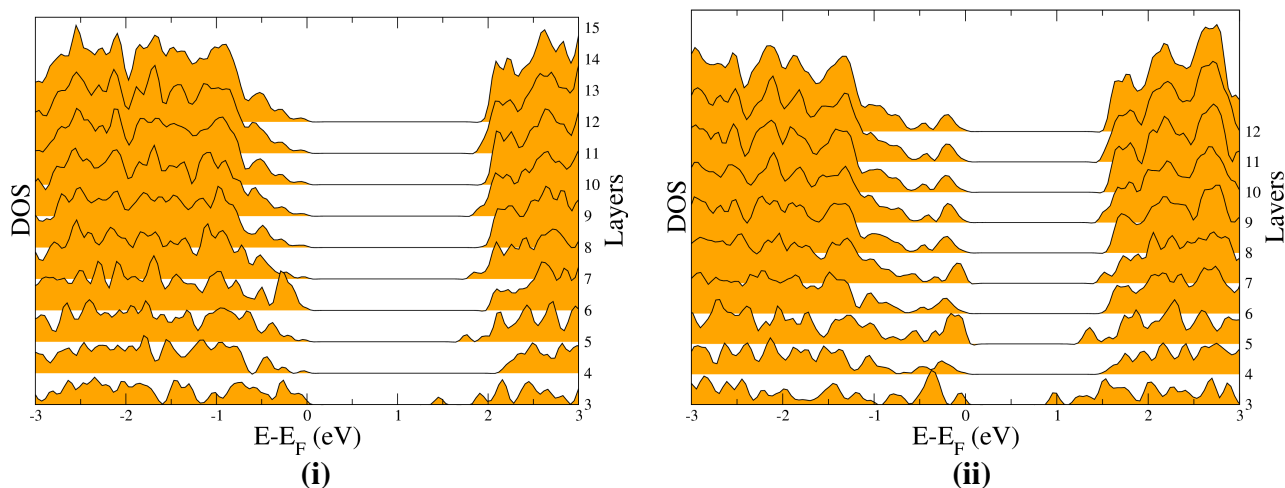
Figure 3: Rutile (110) density of states: Convergence of DOS with slab thickness for **(i)** fully relaxed (FR) and **(ii)** bottom layer fixed slabs (BF).

opt to use a 4 layer slab with the bottom layer fixed for calculation of adsorption energies, as the the correct ordering is maintained and the relative adsorption strengths are reasonably well converged. For the calculation of density of states we use a 4 layer fully relaxed slab, which exhibits a well converged band-gap close to the expected GGA result.

A further point to note is that rutile (110) is also known to form a 1×2 reconstruction following annealing at ~1100K[45]. However, in the formation of (110) dominated rutile nanorod DSSCs, the electrodes are annealed at $\sim$ 400-700K[22,42] and thus we restrict our examination to the 1×1 surface.

Adsorption of Acidic Anchors

As mentioned previously the dye-semiconductor interaction is of fundamental importance to the science of DSSCs. Strong binding of the sensitising dye to the TiO_2 is essential for device stability, and this interaction proceeds mainly through the anchoring moiety. Similarly for efficient charge injection good electronic overlap of the dye and TiO_2 electronic states is required, upon which the anchoring group will have a significant bearing. Typically DSSCs utilise a carboxylic acid

binding strategy, and while other anchoring groups have been used (and in some cases shown more desirable traits than their carboxylic acid analogues) the interaction of other anchoring groups with the increasingly important rutile (110) and anatase (001) surfaces have been much less rigorously examined. Previous works have examined formic acid adsorption on all three of these surfaces[46–48] and previous theoretical work has been done examining the adsorption of phosphonic acid on anatase (101) and rutile (110)[49,50]. To the best of our knowledge at the time of writing no reports have been made on the binding of phosphonic acid to the (001) surface, and no reports have been made on the adsorption of the boronic acid group on any of these three surfaces.

All three of these acidic binding groups can be seen in figure 4. While previous theoretical works have examined formic and phosphonic anchors on some of these surfaces, we repeat all of the calculations so that direct like for like comparisons may be made between systems that have already been examined and those that have not.
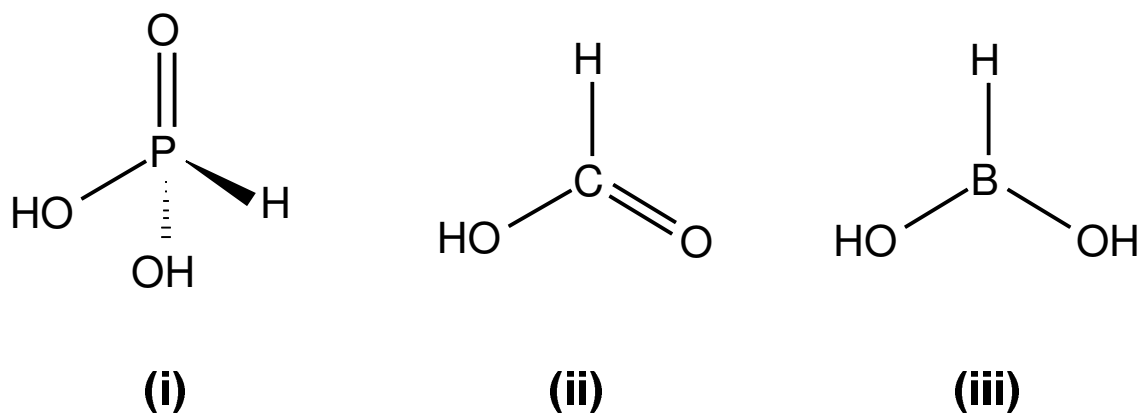

Figure 4: Acidic binding groups examined: (i) Phosphonic acid, (ii) Formic acid and (iii) Boronic acid.

All of these anchoring groups will have several different possible binding motifs with the TiO_2 surfaces, and in order to gauge the strength of interaction and find the most stable structure we must survey several of these possiblities. Some of the potential binding mechanisms of acidic anchors to TiO_2 are schematically illustrated in figure 5. Several of the binding motifs require the dissociation of the acid, in which case the dissociated hydrogen is adsorbed on a nearby undercoordinated
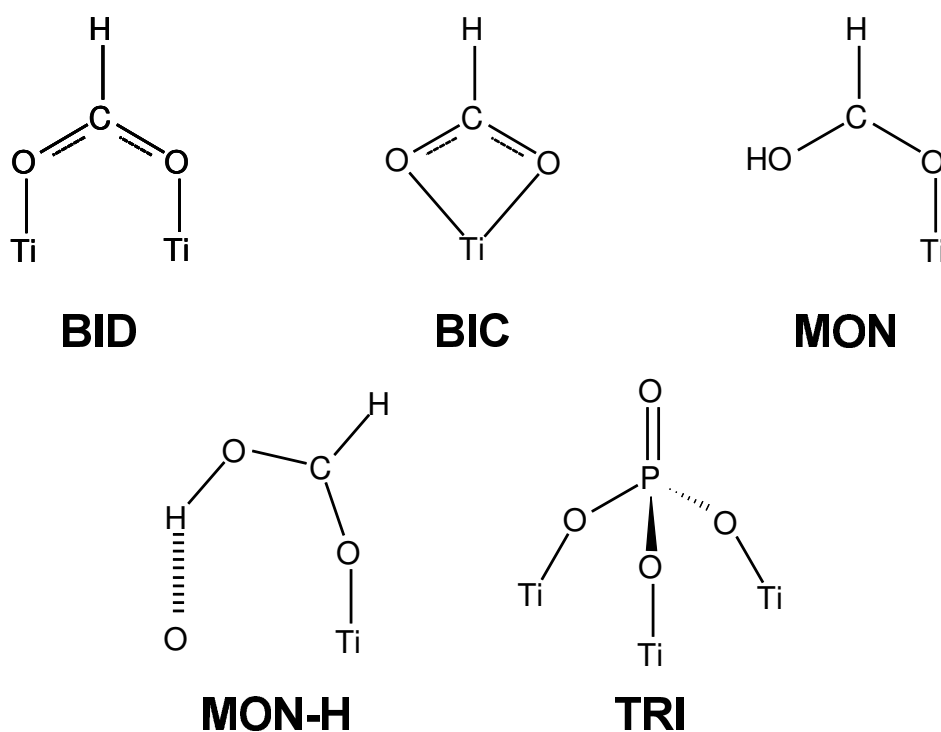
surface oxygen atom (not shown in the figure).

Figure 5: Binding Structures for Acidic Groups: Bidentate (BID), Bidentate-chelating (BIC), Monodentate (MON), Monodentate with hydrogen bond (MON-H) and Tridentate (TRI)(Phosphonic acid is the only anchor for which the tridentate mode is possible)

Calculation of binding energy between the acidic groups and the TiO_2 surfaces proceeds by taking a clean, relaxed surface slab and introducing the anchor molecule in an appropriate binding motif. The strength of the interaction is then calculated by subtracting the energy of the clean surface and the molecule from that of the total system:

$$E_{ADS} = E_{TOT} - (E_{SURF} + E_{MOL}) \qquad (2)$$

In all instances the molecular energy is calculated for the molecule in isolation residing in a cell of dimensions the same as that of the composite system. Similarly the K-point sampling and energy cut-off are maintained constant for each of these calculations.

Anatase (101)

Calculated adsorption energies for all three acidic binding groups in several of the binding structures on the anatase (101) surface can be seen in table 5, and the most stable binding structures are exhibited in figure 6.

Our results illustrate that formic acid binds most strongly in the bidentate bridging mode, with the oxygens bonding to two adjacent Ti(5) surface atoms. An almost equivalent binding energy is obtained for the monodentate binding mode with a hydrogen bond (MON-H) to the nearest O(2) atom. A second monodentate binding mode is reported in which the hydrogen forms a weak bond with a O(3) surface atom (MON), with the adsorption energy being comparatively reduced. Finally the bidentate chelating mode (BIC) is found to be stable, but considerably less so than the monodentate and bridging modes.

Experimentally Fourier transform infrared spectroscopy report the coexistence of two different adsorption structures, a bidentate mode and an unsymmetrical structure[51]. This is in agreement with our result that the monodentate and bidentate bridging modes are energetically similar and likely to coexist. Previous theoretical work has found the most stable structure to be the bidentate bridging mode, with the interaction of the hydrogen bonded monodentate mode extremely similar energetically[46].

Table 5: Calculated adsorption energies for acids on the Anatase (101) surface (in eV.)

Adsorbate	MON	MON-H	MON-2H	BIC	BID	BID-H
Boronic	N/A	-0.72	N/A	+0.12	-0.82	N/A
Formic	-0.71	-1.02	N/A	-0.12	-1.03	N/A
Phosphonic	-1.29	N/A	-1.69	-0.48	N/A	-1.82

The phosphonic acid group has an extra degree of freedom in terms of its binding modes over formic and boronic acids, due to the extra oxygen atom it possesses. Numerous adsorption structures of similar binding modes are therefore available to it, and we report only the most stable of each of these. Examining the results for phosphonic acid we see that overall it binds much
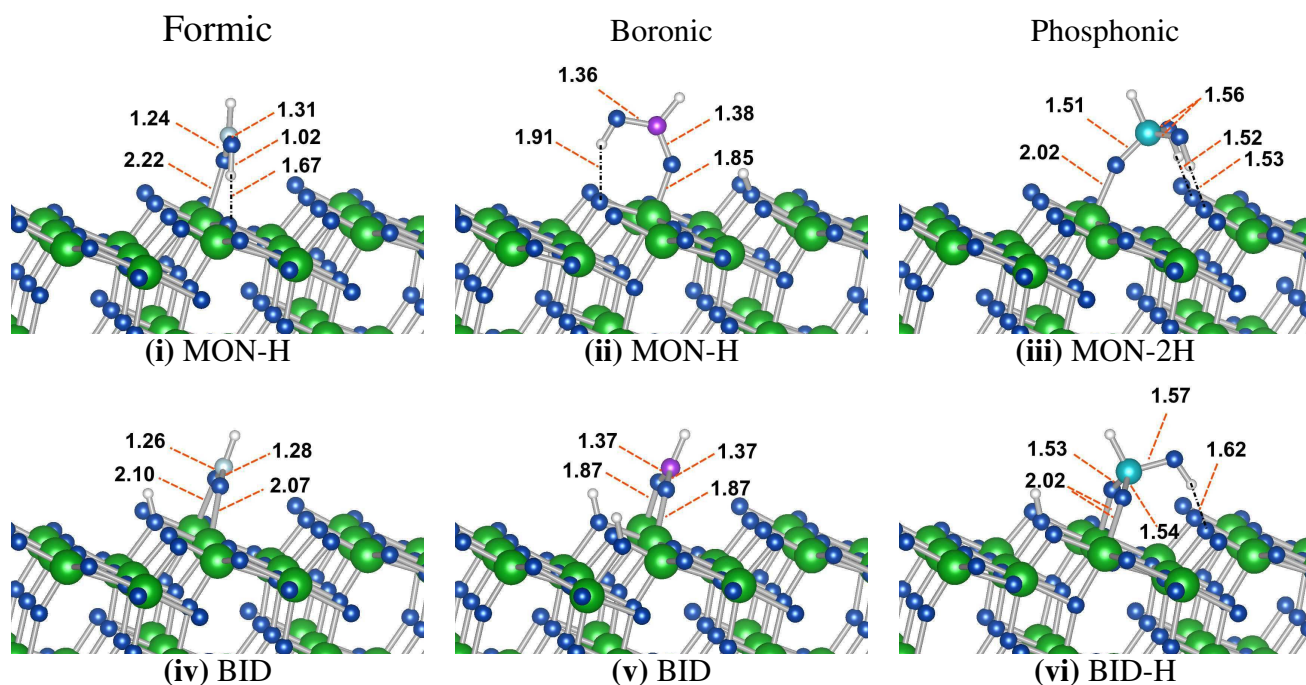
Figure 6: Anchor adsorption structures on anatase (101): Two most stable adsorption structures for formic acid (**(i)** & **(iv)**), boronic acid (**(ii)** & **(v)**) and phosphonic acid (**(iii)** & **(vi)**)

more strongly to the surface in each of the given binding modes than the other acids. The most stable adsorption mode for phosphonic acid is the bidentate bridging mode with an additional single hydrogen bond (BID-H Figure 6), in which two oxygen atoms of the acid group form bonds to two adjacent Ti(5) atoms in the surface, and the final OH group forms a hydrogen bond to an adjacent O(2) atom. A second comparably stable adsorption mode is found where the phosphonic acid binds through its carbonyl group, with the two OH groups forming hydrogen bonds to two adjacent O(2) atoms (MON-2H Figure 6). Previous studies have found similar results, with a DFT tight binding study finding the BID-H to be the most stable with the MON-2H structure being the only stable monodentate structure found after relaxation[49]. A second study found the two to be comparable in energy, but with the monodentate structure slightly more stable by 0.13 eV[50]. Our calculations do obtain further stable monodentate structures, all of which contain a single hydrogen bond irrespective of whether the hydrogen dissociates to reside on the nearest O(2) of the surface or not. Similarly to the previous works no stable tridentate binding mode was obtained.

Chemical adsorption of the boronic acid requires the dissociation of at least one hydrogen atom from either of its OH groups. From the results reported in table 5 we can see that its most stable structure is the bidentate bridging mode, similar to that of both the formic and phosphonic acid groups. However the strength of the interaction for this mode, and for all others, is found to be significantly weaker than that of the formic acid and phosphonic acid groups. While it is still possible for the boronic acid group to form a stable bond with the (101) surface, and therefore anchor dyes to the TiO_2 electrode, it will have poorer device stability and dye take up over dyes anchoring through phosphonic and formic acid groups. Given that the typical nanoparticle DSSC electrode is dominated by the (101) anatase surface this result explains the experimentally observed trend [18], that TiO_2 sensitised with boronic acid groups gave low surface coverage, and resulting low IPCE values. Increasing the number of boronic anchoring moieties had the effect of increasing the surface coverage, and consequently the IPCE.

Stabilisation of the monodentate binding modes through hydrogen bond formation is another interesting feature, with the monodentate modes of both the formic and phosphonic groups being stabilised in such a way. Boronic acid also tended towards the formation of these hydrogen bonds when adsorbed in each of the monodentate modes investigated (again only the most stable of these is reported).

Rutile (110)

Examining the interaction of our binding groups with the rutile (110) surface (table 6) a different trend with respect to the interactions on the anatase (101) surface is immediately observed; in the most stable binding mode the interaction of all three anchoring moieties with rutile (110) is considerably stronger than that with anatase (101). Our direct comparison of adsorption energies illustrates this trend, which in some sense has been reported by proxy when comparing previous studies for formic acid adsorption on the (110) and (101) surfaces [46,52] and for phosphonic acid [20,50]. The two most stable binding structures for each of the anchors on the (110) surface can be seen in figure 7.

Table 6: Calculated adsorption energies for acids on the Rutile (110) surface (in eV.)

Adsorbate	MON	MON-H	BIC	BID	BID-H
Boronic	-0.73	-1.01	+0.53	-1.13	N/A
Formic	-0.71	-1.03	-0.22	-1.36	N/A
Phosphonic	N/A	-1.54	-0.60	N/A	-2.05

As with the anatase (101) surface, for each anchoring group the bidentate bridging mode is again found to be the most stable structure. However there is a contrast when comparing the relative stabilities of each mode, as on the (110) rutile surface the bidentate bridging mode is considerably more stable than the most stable monodentate modes, with perhaps the exception of the boronic anchor for which the bidentate mode is more stable by around 0.15 eV. Experimentally FTIR studies also find one binding mechanism for formate on rutile (110), which is identified as being the bidentate bridging mode by Hartree-Fock studies[53].
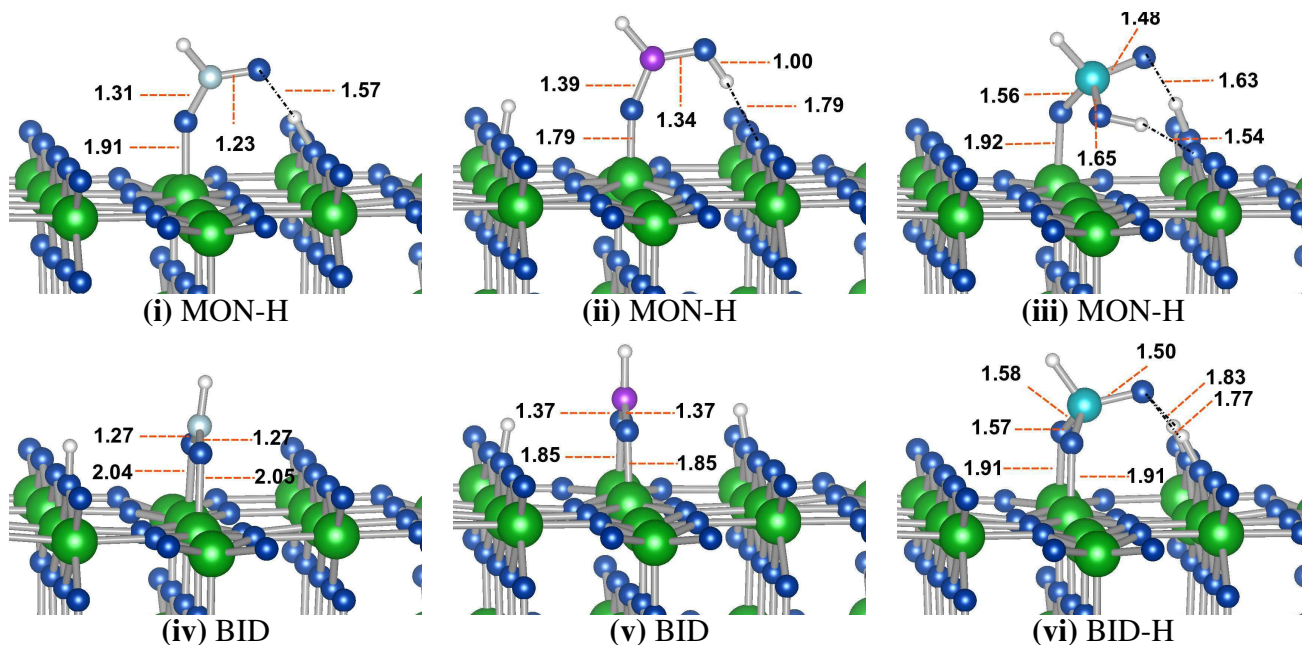

Figure 7: Anchor adsorption structures on rutile (110): Bidentate and monodentate structures for formic acid (**(i)** & **(iv)**), boronic acid (**(ii)** & **(v)**) and phosphonic acid (**(iii)** & **(vi)**)

We note that the relative binding stabilities maintain the same order as the anatase (101) surface,

such that phosphonic > formic > boronic. This is a significant result, suggesting that dyes containing phosphonic acids will again have the ability to bind more strongly than carboxylic anchored dyes when adhering to the majority (110) surface exposed in rutile nanorod electrodes.

Both the formic and boronic acids bind in a very similar manner in their most stable modes, as can seen in figure 7. Addition of a hydrogen bond is found to stabilise the adsorption structure for the boronic and formic anchor. The phosphonic acid again differs in its binding modes slightly, due to its different molecular structure, and has more scope for forming hydrogen bonds than the other two anchors. In both of the phosphonic adsorption modes shown in 7, two hydrogen bonds are formed. Two dissociated hydrogen atoms, attached to O(2) surface atoms, coordinate to the single carbonyl group on the phosphonic acid in BID-H. In MON-H the hydrogen on the phosphonic OH group coordinates to a single O(2) atom, along with the carbonyl group coordinating to the dissociated hydrogen. Similarly to the (101) surface no stable tridentate mode is found rather, when attemping to bind the phosphonic group in a tridentate structure, relaxation returns the mode to a BID-H structure.

Anatase (001)

Similarly to the rutile (110) surface, the anatase (001) surface reconstructs to form a (1×4) termination in order to minimise the surface energy[54], and thereby becoming less reactive. Capping with hydrofluoric acid results in a fluorine terminated (1×1) surface which is more stable than the (101) surface. Using this capping agent it is possible obtain single crystals with extremely high percentages of the (001) surface exposed. There is some debate over whether the (001) surface retains its (1×1) termination after removal of the fluorine capping agent by thermal processing. Experimentally the crystals are reported as remaining unchanged[55], with a recent theoretical work showing that the process of removing the fluorine capping agent will result in the formation of the (1×4) reconstruction[56]. We report here only results on the (1×1) surface termination, and view the study on the (1×4) reconstruction as an important future extension of the work.

Calculated adsorption energies for all three anchors on the (001) surface can be seen in table

21

Table 7: Calculated adsorption energies for acids on the Anatase (001) surface (in eV.)

Adsorbate	MON-H	BIC	BID	BID2	TRI
Boronic	-1.69	-0.65	-0.66	-4.08	N/A
Formic	-1.96	-1.70	-0.73	-1.72	N/A
Phosphonic	-2.70	-1.82	-2.85	-3.21	-2.99

7, along with selected adsorption structures in figure 8. Bidentate bridging can occur in two ways when the anchor binds to two Ti(5) atoms in the corrugated surface, with the anchor either bound above the O(2) atom (labelled BID in table 7) , or above the O(3) atom in the surface (labelled BID2 in table 7). Binding above the O(3) atom results in a more stable structure than when doing so above the O(2) surface atom, this is as a result of the associated stress when the outward corrugation of the O(2) atom is reversed as a result of repulsion from the anchor binding above it.
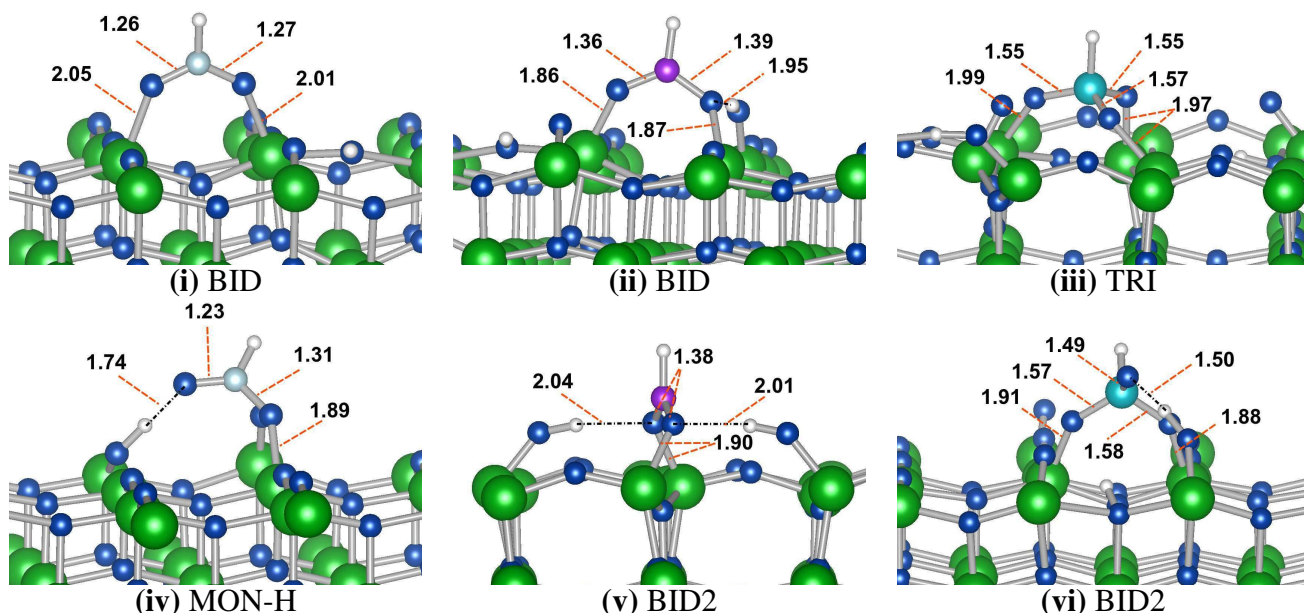

Figure 8: Anchor adsorption structures on anatase (001): Most stable adsorption structures for formic acid (**(i)** & **(iv)**), boronic acid (**(ii)** & **(v)**) and phosphonic acid (**(iii)** & **(vi)**)

High adsorption energies are indicative of the high reactivity of the (001) surface. This can also be seen in the tendency of the O(2) atoms to form surface -OH groups on addition of dissociated

hydrogen atoms (see for example the boronic binding motifs in figure 8), a feature not present in either rutile (110) or anatase (101) surfaces. Another noticeable trait is the stabilisation of the bidentate chelating mode.

For the formic acid adsorption the monodentate structure is now found to be the most stable, with the bidentate bridging mode again reasonably similar in energy, as it was for the (101) surface. However the chelating mode is now also found to be similar energetically. All three modes are more stable than on both the the anatase (101) and rutile (110) surfaces.

In the case of the phosphonic and boronic acids the most stable structures are again found to be the bidentate bridging modes (BID2). The phosphonic acid has numerous significantly stable binding structures of similar adsorption energy. The boronic acid group also has several stable binding structures, however the most stable bidentate mode (BID2) is significantly more energetically favoured than the next most stable (MON-H)

Looking at figure 8(v) the BID2 mode for boronic anchor has, in addition to the usual bidenate O-Ti bond, the two dissociated hydrogen atoms, which have formed surface OH groups, also coordinating to the binding oxygen atoms. This goes some way to explain the stability of the system; moving one of these co-ordinating H-atoms to another O(2) atom further from the adsorbate, and thereby preventing it from forming a hydrogen bond with the binding oxygen atom, results in a 0.88 eV less stable structure.

For the (001) surface we have the important result that a reorganisation of the most stable binding anchors occurs for this surface, giving us boronic > phosphonic >> formic, illustrating that *most* used carboxylic anchor is therefore predicted to have the *least* stable binding structure for the (001) surface and that the *least* used boronic anchor is predicted to have a *significantly stronger* binding structure than both phosphonic and formic acids.

We recognise the importance of performing these calculations on the reconstructed surface, in order to verify the impressive stability of the boronic-(001) surface coupling. However, irrespective of this, our results highlight a significant point when designing dyes for DSSCs; the anchor choice should necessarily depend on the majority surface exposed in the electrode. This is a particularly

important point to consider at present, given the current trend of exploring and exploiting the properties of other electrode TiO_2 morphologies for which the (101) is no longer the dominant exposed surface. As a final point, the impressive binding of the boronic and phosphonic anchors to the unreconstructed (001) surface can be seen as making a strong case for experimentalists to find a way of exploiting its reactivity by functionalising the surface before any reconstruction can occur.

Dye Adsorption

Electronic structure in the composite dye-TiO_2 system forming a DSSC will underpin the device efficiency. Adsorption of carefully selected dyes on a mesoporous TiO_2 electrode will introduce occupied states in the band-gap of TiO_2. Reducing the effective band-gap of the system in this manner thereby provides a photoexcitation pathway for photons which fall outside of the UV range of TiO_2. Among other factors, the relative postition of the dye localised frontier orbitals with respect to those of the TiO_2 electrode will have a significant role in defining the open circuit voltage and therefore the device efficiency. Altering the anchoring group will necessarily change the electronic structure of the dye, and may therefore affect the postitioning of its electronic levels relative to that of the TiO_2, thereby directly affecting the device efficieny.

In order to gauge the extent that changing the anchoring group in a DSSC will affect the electronic structure, we have performed calculations on a well documented coumarin based dye, named NKX-2311[57–60], adsorbed on each of our three TiO_2 surfaces. NKX-2311 utilises the carboxylic acid binding moiety, allowing us to exmaine the effect of using a differing anchor by simply replacing the anchoring group with either the phosphoric or boronic anchors. The chemical structures for NKX-2311 and the same coumarin dye utilising the phosphoric and boronic anchors, which we name NKX-2311P and NKX-2311B respectively, can be seen in figure 9.
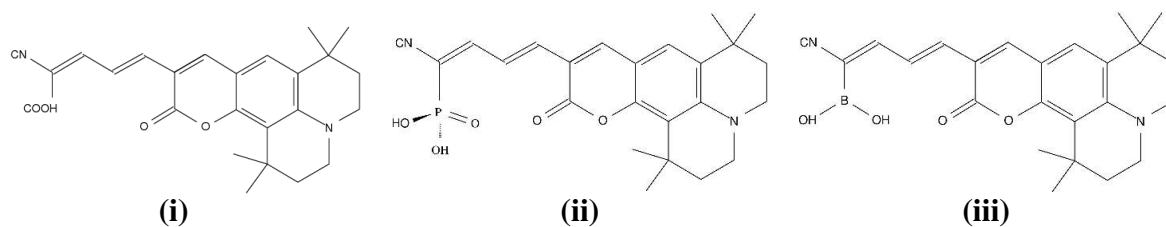
Figure 9: Chemical structures for the adsorbed dye molecules:(i) NKX-2311, (ii) NKX-2311P, (iii) NKX-2311B

Anatase (101)

For each surface we have opted to examine the dyes bound in the strongest adsorption configuration found for each of the isolated anchoring groups from the previous section. In the case of the anatase (101) surface all three anchors were found to bind preferentially in a bidentate bridging mode. Relaxed structures for each of our three dye variants on the (101) surface can be seen in figure 10, along with the calculated adsorption energies.

Examining the adosoption geometries we see that very little difference is found in comparison to the geometry of the respective anchor groups in isolation, and we find that the bond lengths between the anchor and the TiO$_2$ changing only very slightly (the largest change is $\sim 2\%$). Each of the dyes is found to bind more strongly to the surface than the anchors in isolation by $\sim 0.1-0.2$ eV. The relative strength of the adsorption interaction remains the same as that of the isolated anchors, with NKX-2311P > NKX2311 > NKX-2311B, illustrating that in terms of binding properties alone the phosphonic anchor is most effective on the (101) surface.

In order to examine the electronic overlap between the adsorbed dye and the TiO$_2$ lattice we have generated partial density of states plots (PDOS), along with the projection on the adsorbed dyes, which can be seen in figure 11. Examining the PDOS we see that all three dyes introduce dye localised states in the gap, as well as in the conduction band. Previous theoretical work on the NKX-2311 dye adsorbed on a TiO$_2$ cluster calculated the HOMO to dye localised LUMO energy difference as being 1.425eV[59]. Here we obtain a simliar value of ~ 1.4 eV. Comparing the PDOS for NKX-2311 and NKX-2311P we can see that for this surface there is only a marginal

25

$E_{Ads} = -1.11$ eV $\qquad\qquad E_{Ads} = -0.91$ eV $\qquad\qquad E_{Ads} = -1.88$ eV

(i) $\qquad\qquad\qquad\qquad$ (ii) $\qquad\qquad\qquad\qquad$ (iii)
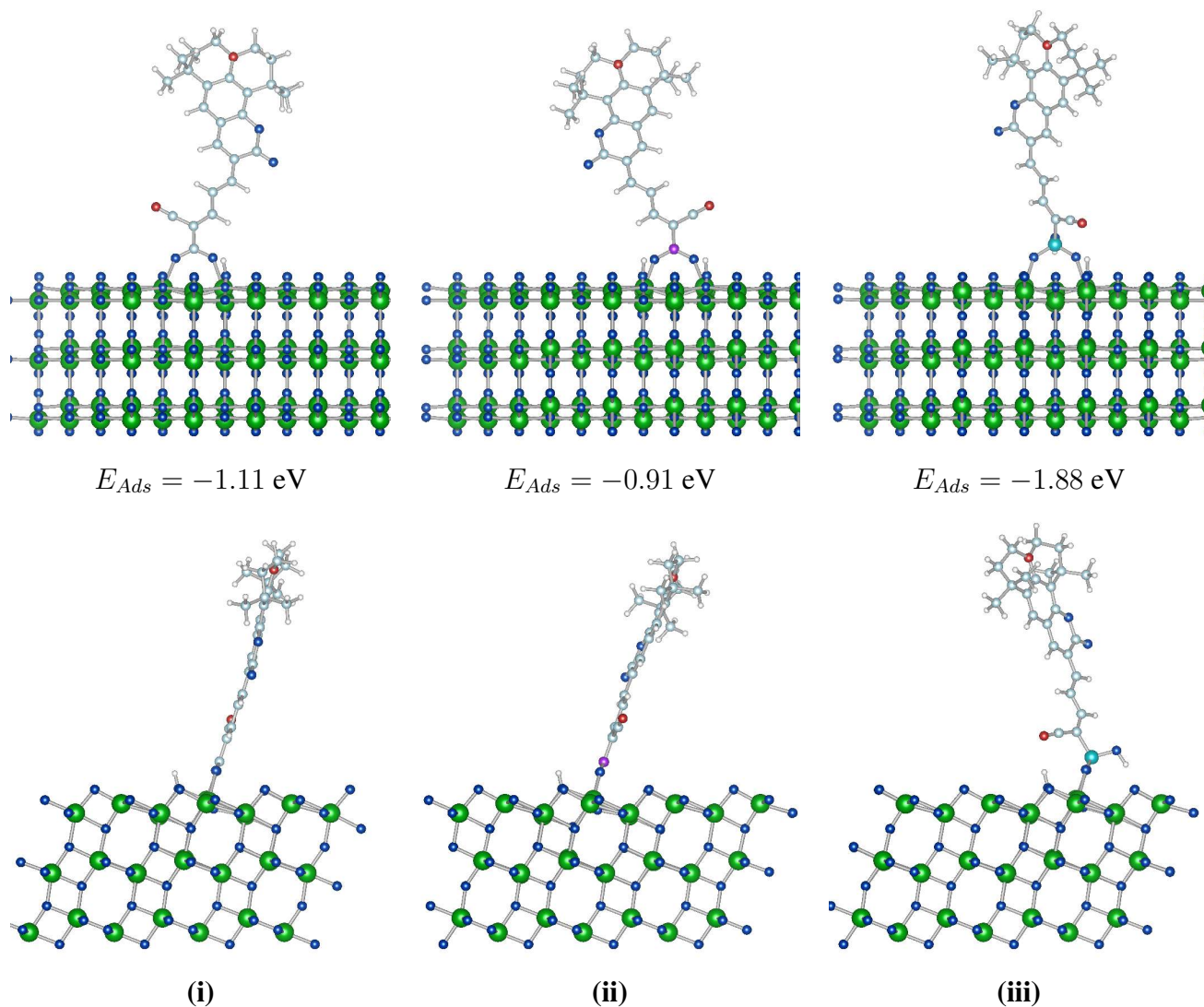
Figure 10: Relaxed dye adsorption geometries on Anatase (101): **(i)** NKX-2311, **(ii)** NKX-2311B and **(iii)** NKX-2311P. Front (top) and side (bottom) perspectives are shown.

change in the electronic structure as a result of using a phosphonic anchoring group. The highest occupied molecular orbital (HOMO) is dye localised in both cases, and resides around 0.5 eV below the TiO$_2$ conduction band. Further dye localised states are introduced at around the same energy ($\sim 0.1 - 0.3$ eV) above the valence band in both cases.

In the case of the boronic anchor we have a markedly different electronic structure; relative shifts of the dye localised states occur both within the TiO$_2$ band-gap and with respect to each other, with the result that a further dye localised state is introduced into the gap. It is also worth noting that the HOMO is found to reside essentially at the bottom of the band-gap, with the composite system ostenibly acting as a conductor. However, semi-local GGA density functional theory is known to underestimate the band-gap in semiconductors, as a result of a lack of the discontinuity in the exchange-correlation potential[61]. This results in our calculated band-gap being ~ 2 eV as opposed to the experimentally reported value of 3.2 eV.

Bearing this point in mind, and given that DFT is a ground state theory we now discuss the possible consequences of the electronic structure on DSSC efficiency. At face value the remarkably similar electronic structure of the NKX-2311P and NKX-2311 dyes would suggest that they would be likely to have similar device properties. However examining the dye localised LUMO states (LDOS*) in the right hand side of figure 11 we see that the NKX-2311 LDOS* is considerably more extended throughout the TiO$_2$ conduction band. Charge injection times will depend upon the electronic overlap between the TiO$_2$ and dye orbitals, suggesting that the carboxylic anchor bound dye will have a more efficient injection mechanism that the NKX-2311P and NKX-2311B dyes. This result agrees with previous work examining the effect of the anchoring group on the adsorption of a pyridine molecule[62], in which the carboxylic acid bound molecule was found to have a larger full width at half maximum value for the dye localised LUMO. Experiments have also been found this to be the case, with more efficient charge injection through the carboxylic anchoring group[63,64]. While this more efficient injection does not necessarily automatically result in higher efficiencies for all carboxylic bound dyes, it has certainly shown to be the case for some dye groups[64,65].

For NKX-2311B we can note that despite the lower binding energy to the (101) surface, and similar LUMO* overlap as NKX-2311P, the extra introduced dye localised state in the band-gap is significant. Increasing the number of excitation pathways, by this introduction of a new gap state, may lead to an increase in the short-circuit current, J_{SC}, and to an increase in device efficiency over NKX-2311P.
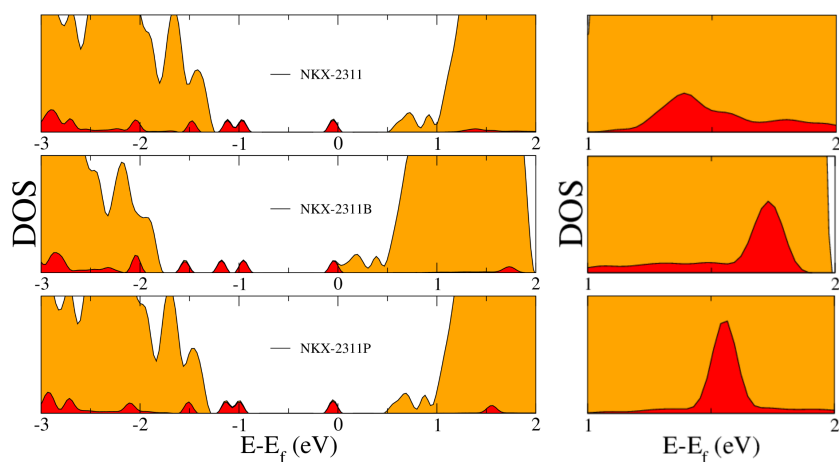

Figure 11: Projected density of states for dyes adsorbed on the anatase (101) surface. Top: NKX-2311, Middle: NKX-2311B, Bottom: NKX-2311P. Total DOS in orange, with the dye localised PDOS in red. On the right hand side the LUMO* is enlarged for clarity.

Rutile (110)

For the rutile (110) surface, the dye binding geometries are again very similar to that of the isolated anchor groups, as seen in the relaxed adsorption structures shown in figure 12. The ordering of the relative strengths of the interaction is maintained (also shown in figure 12) with NKX-2311P > NKX-2311 > NKX-2311B, which again illustrates that the phosphonic acid anchor is the most

attractive in terms of binding properties alone. More generally we note that each of the dyes bind more strongly to the (110) rutile surface than the anatase (101).

Examining the electronic properties in figure 13 we can see that as opposed to the anatase (101) surface the electronic structre for the NKX-2311P dye now follows that of the NKX-2311B dye, with shifted states in the gap relative to the NKX-2311 dye. This again has the effect of introducing an extra state in the gap about $0.3eV$ above the valence band for both of these dyes, with the HOMO just below the calculated conduction band. For the NKX-2311 dye the HOMO is further from the conduction band, and there are fewer states in the gap. As with the boronic anchored dye on the (101) surface this may again have the effect of increasing the number of excitation pathways for the boronic and phosphonic anchored dyes over the formic anchor, and lead to higher J_{SC} values. This different behaviour of the phosphonic anchored dye on the rutile (110) as opposed to the anatase (101) surface is an interesting result illustrating that, as with the isolated anchor groups, there are considerable differences between the results on alternative TiO_2 surfaces.

Examining the LUMO[*] states we again see that the NKX-2311 dye has a larger number of dye localised states well spread out within the TiO_2 conduction band. As with these dyes on the (101) surface this significant overlap would suggest that the carboxylic acid anchor may have the most efficient charge injection mechanism.

Anatase (001)

Relaxed structures for the NKX-2311 dyes on the anatase (001) surface, along with the calculated adsorption energies, may be seen in figure 14. Very similar structures to those of the isolated anchors are again found for the formic and boronic bound dyes, with relevant bond lengths for the anchors to the surface changing by at most a few hundredths of an Angstrom. However the binding structure of the NKX-2311P dye has a couple of considerable differences with respect to that of the isolated anchor. While for the isolated anchor the carbonyl group formed a hydrogen bond to one of the dissociated hydrogen atoms, in this case this hydrogen atom has reassociated to the carbonyl group. Similarly this reassociation of surface hydrogen has been shown to provide a

$E_{Ads} = -1.74$ eV $\qquad\qquad$ $E_{Ads} = -1.53$ eV $\qquad\qquad$ $E_{Ads} = -2.26$ eV

(i) $\qquad\qquad\qquad\qquad$ **(ii)** $\qquad\qquad\qquad\qquad$ **(iii)**
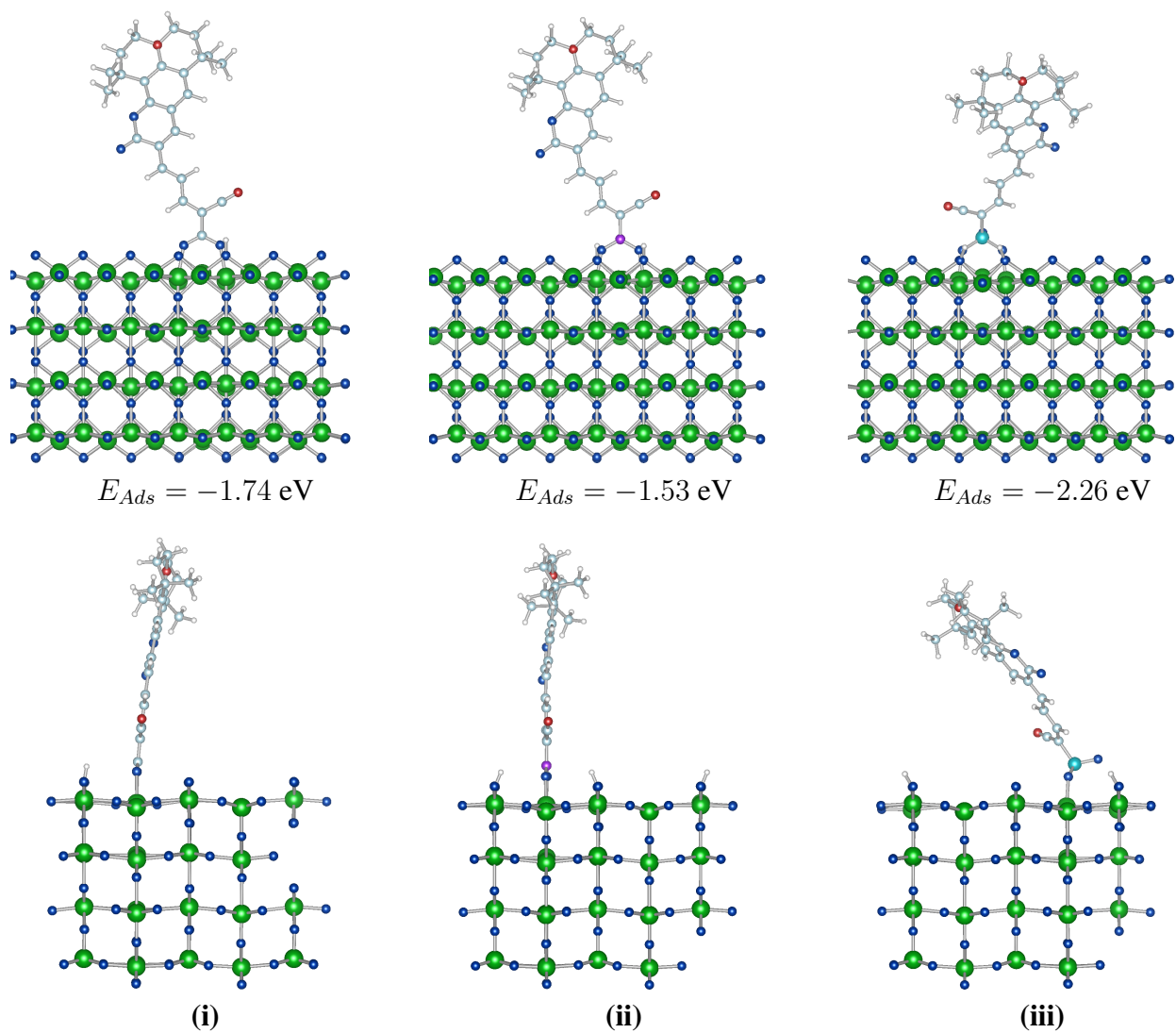
Figure 12: Relaxed dye adsorption geometries on Rutile (110): **(i)** NKX-2311, **(ii)** NKX-2311B and **(iii)** NKX-2311P. Front (top) and side (bottom) perspectives are shown.
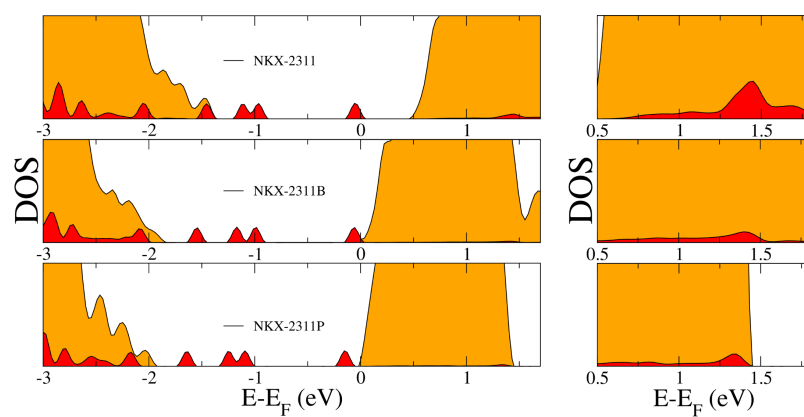
Figure 13: Projected density of states for dyes adsorbed on the rutile (110) surface. Top: NKX-2311, Middle: NKX-2311B, Bottom: NKX-2311P. Total DOS in orange, with the dye localised PDOS in red. On the right hand side the LUMO* is enlarged for clarity.

stabilising effect for dyes binding to the anatase (101) surface[66]. The second dissociated hydrogen atom has been transferred on the surface from a O(3) atom to an O(2) atom, breaking a Ti-O bond, with this hydroxyl group in turn forming a hydrogen bond with the OH group of the anchor.

Examining the adsorption energies we see that there is a considerable stabilisation of both the NKX-2311 and NKX-2311P dyes over the isolated anchor groups. It is likely that this stabilisation for the NKX-2311P dye may be attributed in part to this reorganisation and reassociation of the hydrogen groups on the surface. On closer examination of the geometry for the NKX-2311 dye we find that, although the bonds between the anchor and the surface change only very slightly, the Ti atom bonded to the surface OH group has shifted causing the Ti-OH bond length to decrease from 1.94 Å for the isolated dye to 1.74 Å. Subsequent changes in bond lengths occur between this Ti atom and the oxygen atoms of the lattice, which may be responsible for this stabilisation.

While the NKX-2311 and NKX-2311P dyes are stabilised so too is the NKX-2311B dye, albeit much less so, and it remains the most stable anchoring moeity. Again we have the reorganisation of the relative binding strengths with respect to the rutile (110) and anatase (101) surfaces, with NKX-2311B > NKX-2311P >> NKX-2311, highlighting the fact that in terms of binding to the surface the carboxylic acid group is at a considerable disadvantage compared to the boronic and phosphonic anchors.

Partial density of states, along with the projection on the adsorbed dyes, can be seen in figure 15. Once again dye localised states are introduced into the band-gap for all three systems. However these dye localised states are shifted relative to the TiO_2 bands depending on the anchoring group used. For the NKX-2311P dye only one state is located within the gap, with two further dye levels located at the very top of the valence band. On changing the anchor to the carboxylic group for NKX-2311 we see that a shift forces a further state to appear in the gap. Similarly changing to the boronic anchor we see a similar shift introducing a third dye localised state in the gap. Introduction of the extra gap states for the NKX-2311B dye could potentially increase the number permitted photo-excitation pathways in comparison to NKX-2311 and NKX-2311P.

Examining the LUMO* states from our PDOS plots we can see that for the (001) surface the

$E_{Ads} = -2.80$ eV $E_{Ads} = -4.35$ eV $E_{Ads} = -4.26$ eV

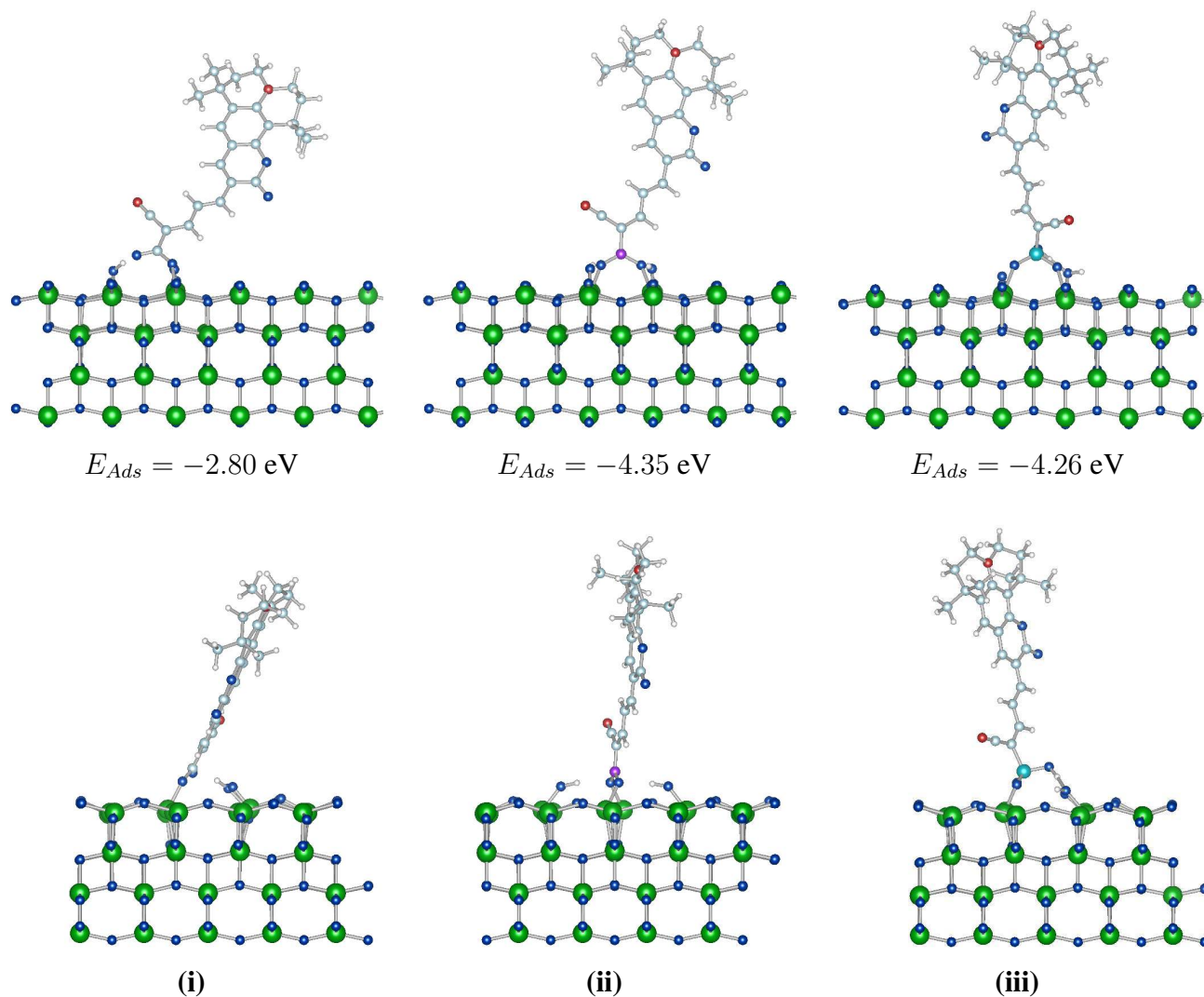**(i)**   **(ii)**   **(iii)**

Figure 14: Relaxed dye adsorption geometries on Anatase (001): **(i)** NKX-2311, **(ii)** NKX-2311B and **(iii)** NKX-2311P. Front (top) and side (bottom) perspectives are shown.

carboxylic acid bound dye now has a very similar overlap with the TiO$_2$ states as the NKX-2311B and NKX-2311P dyes. This would suggest that the electron injection may be similar for all three on the (001) surface. This is an interesting result, which when coupled with the extra states in the gap for the NKX-2311B dye, suggests that NKX-2311B would have a higher J$_{SC}$ than both NKX-2311 and NKX-2311P. Coupling this point with the excellent binding of the NKX-2311B dye suggests that the boronic anchor could be an impressive alternative to the carboxylic anchor for the (001) surface.
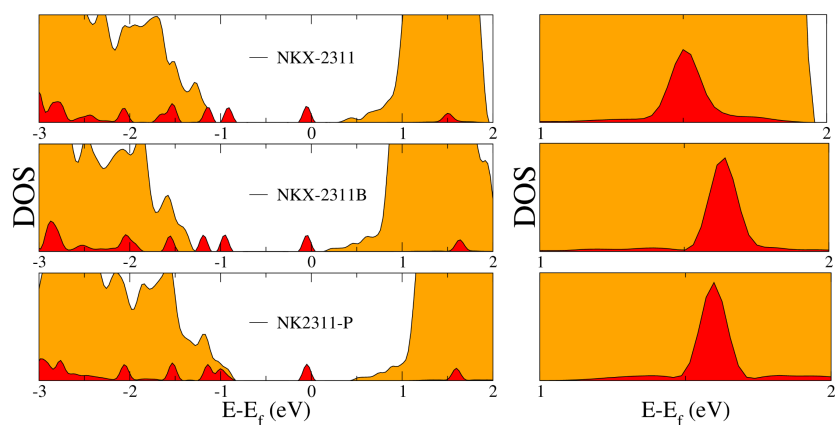
Figure 15: Projected density of states for dyes adsorbed on the anatase (001) surface. Top: NKX-2311, Middle: NKX-2311B, Bottom: NKX-2311P. Total DOS in orange, with the dye localised PDOS in red. On the right hand side the LUMO* is enlarged for clarity.

Conclusions

We have introduced the two main TiO$_2$ polymorphs of interest for use as electrodes in dye sensitised solar cells and characterised three of the most important TiO$_2$ surfaces for use in DSSCs.

Examining the interaction of three binding anchors with each of these surfaces allowed us to compare and contrast the benefits of the most used carboxylic acid group with under-used phosphonic and boronic anchors. Our results show that significant differences exist for the anchors when binding to different surfaces, with considerable stabilisation and reorganisation of the relative binding strengths depending on the surface the anchors adsorb to.

Extending this investigation to examine the effect anchors have when binding dyes to these surfaces, we found similar results. Variation of the anchor group was found to produce considerable differences on the binding strengths and electronic structure of the composite system depending on the surface chosen.

This highlights the important, but often neglected, point; that anchoring groups perform *differently* on different surfaces and that the anchor choice should necessarily depend on the majority surface exposed in the elctrode. Although somewhat obvious, this conclusion is a useful pointer to experimentalists working in the field and is something that should be taken into consideration when designing sensitising dyes. This is a point that is particularly important to consider at present, given the current interest in other TiO_2 electrode morphologies for which the anatase (101) surface is no longer the dominant exposed surface.

Finally the reactivity, and impressive binding strength of the anchors when attaching to unreconstructed anatase (001) surface is found to make a compelling case for experimentalists to exploit this reactivity by functionalising before surface reconstruction, with the boronic and phosphonic anchoring groups in particular showing great promise as anchors when adhereing dyes to this surface.

Acknowledgements

Supporting Information

Most stable adsorption structures are available online[67].

References

(1) Linsebigler, A. L.; Lu, G.; Yates, J. T. *Chemical Reviews* **1995**, *95*, 735–758.

(2) Nakata, K.; Fujishima, A. *Journal of Photochemistry and Photobiology C: Photochemistry Reviews* **2012**, *13*, 169 – 189.

(3) Wang, D. L.; Watson, S. S.; Sung, L.-P.; Tseng, I.-H.; Bouis, C. J.; Fernando, R. *Journal of Coatings Technology and Research* **2011**, *8*, 19–33.

(4) Maness, P.-C.; Smolinski, S.; Blake, D. M.; Huang, Z.; Wolfrum, E. J.; Jacoby, W. A. *Applied and environmental microbiology* **1999**, *65*, 4094–4098.

(5) Mills, A.; Davies, R. H.; Worsley, D. *Chem. Soc. Rev.* **1993**, *22*, 417–425.

(6) amd Michael Grätzel, B. O. *Nature* **1991**, *353*, 737 – 740.

(7) Diebold, U. *Surface Science Reports* **2003**, *48*, 53–229.

(8) Listorti, A.; O'Regan, B.; Durrant, J. R. *Chemistry of Materials* **2011**, *23*, 3381–3399.

(9) K. Nazeeruddin, M.; Pechy, P.; Grätzel, M. *Chem. Commun.* **1997**, 1705–1706.

(10) Nazeeruddin, M. K. et al. *Journal of the American Chemical Society* **2001**, *123*, 1613–1624, PMID: 11456760.

(11) Nazeeruddin, M. K.; Kay, A.; Rodicio, I.; Humphry-Baker, R.; Mueller, E.; Liska, P.; Vlachopoulos, N.; Grätzel, M. *Journal of the American Chemical Society* **1993**, *115*, 6382–6390.

(12) Zhang, H.; F. Banfield, J. *J. Mater. Chem.* **1998**, *8*, 2073–2076.

(13) Lazzeri, M.; Vittadini, A.; Selloni, A. *Phys. Rev. B* **2001**, *63*, 155409.

(14) Vittadini, A.; Selloni, A.; Rotzinger, F. P.; Grätzel, M. *The Journal of Physical Chemistry B* **2000**, *104*, 1300–1306.

(15) Xu, M.; Noei, H.; Buchholz, M.; Muhler, M.; WÃ¶ll, C.; Wang, Y. *Catalysis Today* **2012**, *182*, 12 – 15.

(16) Zakeeruddin, S. M.; Nazeeruddin, M. K.; Pechy, P.; Rotzinger, F. P.; Humphry-Baker, R.; Kalyanasundaram, K.; Grätzel, M.; Shklover, V.; Haibach, T. *Inorganic Chemistry* **1997**, *36*, 5937–5946.

(17) Pechy, P.; Rotzinger, F. P.; Nazeeruddin, M. K.; Kohle, O.; Zakeeruddin, S. M.; Humphry-Baker, R.; Gratzel, M. *J. Chem. Soc., Chem. Commun.* **1995**, *0*, 65–66.

(18) Altobello, S.; Bignozzi, C.; Caramori, S.; Larramona, G.; Quici, S.; Marzanni, G.; Lakhmiri, R. *Journal of Photochemistry and Photobiology A: Chemistry* **2004**, *166*, 91 – 98.

(19) Katono, M.; Bessho, T.; Meng, S.; Humphry-Baker, R.; Rothenberger, G.; Zakeeruddin, S. M.; Kaxiras, E.; Grätzel, M. *Langmuir* **2011**, *27*, 14248–14252.

(20) Nilsing, M.; Persson, P.; Lunell, S.; Ojamäe, L. *The Journal of Physical Chemistry C* **2007**, *111*, 12116–12123.

(21) Thavasi, V.; Renugopalakrishnan, V.; Jose, R.; Ramakrishna, S. *Materials Science and Engineering: R: Reports* **2009**, *63*, 81 – 99.

(22) Lv, M.; Zheng, D.; Ye, M.; Sun, L.; Xiao, J.; Guo, W.; Lin, C. *Nanoscale* **2012**, *4*, 5872–5879.

(23) Lv, M.; Zheng, D.; Ye, M.; Xiao, J.; Guo, W.; Lai, Y.; Sun, L.; Lin, C.; Zuo, J. *Energy Environ. Sci.* **2013**, *6*, 1615–1622.

(24) Laskova, B. et al. *Journal of Solid State Electrochemistry* **2012**, *16*, 2993–3001.

(25) Zhang, H.; Han, Y.; Liu, X.; Liu, P.; Yu, H.; Zhang, S.; Yao, X.; Zhao, H. *Chem. Commun.* **2010**, *46*, 8395–8397.

(26) Yu, J.; Fan, J.; Lv, K. *Nanoscale* **2010**, *2*, 2144–2149.

(27) Kresse, G.; Furthmüller, J. *Computational Materials Science* **1996**, *6*, 15 – 50.

(28) Perdew, J. P.; Chevary, J. A.; Vosko, S. H.; Jackson, K. A.; Pederson, M. R.; Singh, D. J.; Fiolhais, C. *Phys. Rev. B* **1992**, *46*, 6671–6687.

(29) Vanderbilt, D. *Phys. Rev. B* **1990**, *41*, 7892–7895.

(30) Pulay, P. *Chemical Physics Letters* **1980**, *73*, 393 – 398.

(31) Burdett, J. K.; Hughbanks, T.; Miller, G. J.; Richardson, J. W.; Smith, J. V. *Journal of the American Chemical Society* **1987**, *109*, 3639–3646.

(32) Gong, X.-Q.; Selloni, A.; Vittadini, A. *The Journal of Physical Chemistry B* **2006**, *110*, 2804–2811, PMID: 16471889.

(33) Gong, X.-Q.; Selloni, A. *The Journal of Physical Chemistry B* **2005**, *109*, 19560–19562, PMID: 16853530.

(34) Ohno, T.; Sarukawa, K.; Matsumura, M. *New J. Chem.* **2002**, *26*, 1167–1170.

(35) Yu, H.; Tian, B.; Zhang, J. *Chemistry - A European Journal* **2011**, *17*, 5499–5502.

(36) Sun, L.; Zhao, Z.; Zhou, Y.; Liu, L. *Nanoscale* **2012**, *4*, 613–620.

(37) Yu, J.; Fan, J.; Lv, K. *Nanoscale* **2010**, *2*, 2144–2149.

(38) Wu, X.; Chen, Z.; Lu, G. Q. M.; Wang, L. *Advanced Functional Materials* **2011**, *21*, 4167–4172.

(39) Zhang, J.; Wang, J.; Zhao, Z.; Yu, T.; Feng, J.; Yuan, Y.; Tang, Z.; Liu, Y.; Li, Z.; Zou, Z. *Phys. Chem. Chem. Phys.* **2012**, *14*, 4763–4769.

(40) Kang, S.; Choi, S.-H.; Kang, M.-S.; Kim, J.-Y.; Kim, H.-S.; Hyeon, T.; Sung, Y.-E. *Advanced Materials* **2008**, *20*, 54–58.

(41) Jung, Y. H.; Park, K.-H.; Oh, J. S.; Kim, D.-H.; Hong, C. K. *Nanoscale Research Letters* **2013**, *8*, 37.

(42) Guo, W.; Xu, C.; Wang, X.; Wang, S.; Pan, C.; Lin, C.; Wang, Z. L. *Journal of the American Chemical Society* **2012**, *134*, 4437–4441.

(43) Kiejna, A.; Pabisiak, T.; Gao, S. W. *Journal of Physics: Condensed Matter* **2006**, *18*, 4207.

(44) Lindsay, R.; Wander, A.; Ernst, A.; Montanari, B.; Thornton, G.; Harrison, N. M. *Phys. Rev. Lett.* **2005**, *94*, 246102.

(45) Onishi, H.; Iwasawa, Y. *Surface Science* **1994**, *313*, L783 – L789.

(46) Nunzi, F.; De Angelis, F. *The Journal of Physical Chemistry C* **2011**, *115*, 2179–2186.

(47) Gong, X.-Q.; Selloni, A.; Vittadini, A. *The Journal of Physical Chemistry B* **2006**, *110*, 2804–2811, PMID: 16471889.

(48) Bates, S.; Kresse, G.; Gillan, M. *Surface Science* **1998**, *409*, 336 – 349.

(49) Luschtinetz, R.; Frenzel, J.; Milek, T.; Seifert, G. *The Journal of Physical Chemistry C* **2009**, *113*, 5730–5740.

(50) Nilsing, M.; Lunell, S.; Persson, P.; Ojamäe, L. *Surface Science* **2005**, *582*, 49 – 60.

(51) Popova, G.; Andrushkevich, T.; Chesalov, Y.; Stoyanov, E. *Kinetics and Catalysis* **2000**, *41*, 805–811.

(52) Käckell, P.; Terakura, K. *Surface Science* **2000**, *461*, 191 – 198.

(53) Rotzinger, F. P.; Kesselman-Truttmann, J. M.; Hug, S. J.; Shklover, V.; Grätzel, M. *The Journal of Physical Chemistry B* **2004**, *108*, 5004–5017.

(54) Herman, G. S.; Sievers, M. R.; Gao, Y. *Phys. Rev. Lett.* **2000**, *84*, 3354–3357.

(55) Yang, H. G.; Sun, C. H.; Qiao, S. Z.; Zou, G., Jinand Liu; Smith, S. C.; Cheng, H. M.; Lu, G. Q. *Nature* **2007**, *453*, 638–641.

(56) Selcuk, S.; Selloni, A. *The Journal of Physical Chemistry C* **2013**, *117*, 6358–6362.

(57) Hara, K.; Sato, T.; Katoh, R.; Furube, A.; Ohga, Y.; Shinpo, A.; Suga, S.; Sayama, K.; Sugihara, H.; Arakawa, H. *The Journal of Physical Chemistry B* **2003**, *107*, 597–606.

(58) Frontiera, R. R.; Dasgupta, J.; Mathies, R. A. *Journal of the American Chemical Society* **2009**, *131*, 15630–15632, PMID: 19860478.

(59) Sanchez-de Armas, R.; San Miguel, M. A.; Oviedo, J.; Sanz, J. F. *Phys. Chem. Chem. Phys.* **2012**, *14*, 225–233.

(60) Oviedo, M. B.; Zarate, X.; Negre, C. F. A.; Schott, E.; Arratia-PÃ©rez, R.; SÃ¡nchez, C. G. *The Journal of Physical Chemistry Letters* **2012**, *3*, 2548–2555.

(61) Perdew, J. P.; Levy, M. *Phys. Rev. Lett.* **1983**, *51*, 1884–1887.

(62) Nilsing, M.; Persson, P.; Ojamäe, L. *Chemical Physics Letters* **2005**, *415*, 375 – 380.

(63) Ernstorfer, R.; Gundlach, L.; Felber, S.; Storck, W.; Eichberger, R.; Willig, F. *The Journal of Physical Chemistry B* **2006**, *110*, 25383–25391, PMID: 17165985.

(64) Brennan, B. J.; Llansola Portoles, M. J.; Liddell, P. A.; Moore, T. A.; Moore, A. L.; Gust, D. *Phys. Chem. Chem. Phys.* **2013**, *15*, 16605–16614.

(65) Brewster, T. P.; Konezny, S. J.; Sheehan, S. W.; Martini, L. A.; Schmuttenmaer, C. A.; Batista, V. S.; Crabtree, R. H. *Inorganic Chemistry* **2013**, *52*, 6752–6764.

(66) Sodeyama, K.; Sumita, M.; O'Rourke, C.; Terranova, U.; Islam, A.; Han, L.; Bowler, D. R.; Tateyama, Y. *The Journal of Physical Chemistry Letters* **2012**, *3*, 472–477.

(67) `http://dx.doi.org/10.6084/m9.figshare.961771`.